

# Formation of plasma around a small meteoroid: 2. Implications for radar head echo

Y. S. Dimant<sup>1</sup> and M. M. Oppenheim<sup>1</sup>

<sup>1</sup>Center for Space Physics, Boston University

## Key Points:

- Calculates the spatial distribution of the plasma density around a small ablating meteoroid
- Plasma density scales with the collisional mean free path and is independent of the meteoroid velocity
- Provides a basis for realistic modeling of radar head echoes

arXiv:1609.00256v1 [physics.plasm-ph] 1 Sep 2016

## Abstract

This paper calculates the spatial distribution of the plasma responsible for radar head echoes by applying the kinetic theory developed in the companion paper (Dimant and Oppenheim, arXiv:1608.08524). This results in a set of analytic expressions for the plasma density as a function of distance from the meteoroid. It shows that, at distances less than a collisional mean-free-path from the meteoroid surface, the plasma density drops in proportion to  $1/R$  where  $R$  is the distance from the meteoroid center; and, at distances much longer than the mean-free-path behind the meteoroid, the density diminishes at a rate proportional to  $1/R^2$ . The results of this paper should be used for modeling and analysis of radar head echoes.

## 1 Introduction

The radar head echo is a signal that reflects from the plasma surrounding the fast-descending meteoroid and is doppler-shifted by approximately the meteoroid velocity. Only a small volume of the dense plasma sufficiently close to the meteoroid contributes to the corresponding radar wave reflection. Quantitative knowledge of the spatial structure of the near-meteoroid plasma is crucial for accurate modeling the head echo radar reflections [Bronshten, 1983; Ceplecha *et al.*, 1998; Close *et al.*, 2005; Campbell-Brown and Close, 2007].

In the companion paper [Dimant and Oppenheim, 2016], hereinafter referred to as Paper 1, we developed a first-principle kinetic theory of the plasma formed around a small meteoroid as it moves through the atmosphere at hypersonic speeds. Using a number of easily justified assumptions, we obtained approximate analytic expressions describing velocity distributions of meteoric ions and neutrals. In this paper, we calculate the spatial structure of the plasma density that follows from the kinetic theory developed in Paper 1. This calculation demonstrates that this spatial structure differs dramatically from a simple Gaussian or exponential distribution currently employed for modeling radar wave scattering from the meteor plasma [Close *et al.*, 2005; Marshall and Close, 2015]. This research does not describe the distribution of plasma or neutrals in the meteoroid tail where particles lag well behind the meteoroid after having collided more than once.

Simple analysis of individual collisions between particles indicates that heavy meteoric particles in the near-meteor sheath consist predominantly of the ‘primary’ and ‘secondary’ particles. By a primary particle we mean an ablated meteoroid particle that moves freely with a ballistic trajectory until it collides with an atmospheric molecule. These primary particles are predominantly neutral. A secondary particle is a former primary particle that experienced exactly one collision, either scattering or ionizing. Most of the near-meteoroid ions responsible for head echoes belong to the group of secondary particles. The vast majority of ions that experienced multiple collisions since the original ablation lag behind the fast-moving meteoroid and form a long-lived extended column of plasma visible to radars through specular or non-specular echoes.

Given the velocity distributions developed in Paper 1 as a function of spatial coordinates, one can integrate over velocity variables to find the corresponding particle density. However, the complexity of these analytic expressions makes this non-trivial. This paper makes an additional simplifying assumption about the collision model (the isotropic differential cross-section of ionization) and then integrates over the velocities to obtain the meteor gas and plasma density as a function of distance from the meteoroid.

The paper is organized as follows. Section 2 summarizes the results of Paper 1 on the ion distribution function. Section 3 performs the calculations of the near-meteoroid plasma density. Section 4 discusses implications of our theory and some caveats. Section 5 lists the major underlying assumptions and discusses the paper results.

## 2 Summary of the ion distribution function

Paper 1 does all our calculations in the rest frame of a meteoroid moving through the atmosphere with the local velocity  $-\vec{U}$ , so that in this frame the impinging atmospheric particles move with the opposite velocity,  $\vec{U}$ . We define the coordinate system with the major axis passing through the meteoroid center and parallel to  $\vec{U}$ . Due to the axial symmetry about  $\vec{U}$ , we characterize the real space by two spherical coordinates: the radial distance from the meteoroid center,  $R$ , and the polar angle,  $\theta$ , measured from the major axis ( $\theta = 0$  corresponds to the major semi-axis behind the meteoroid, while  $\theta = \pi$  corresponds to the opposite semi-axis in front of it). Figure 1, reproduced from Paper 1, explains all relevant notations.

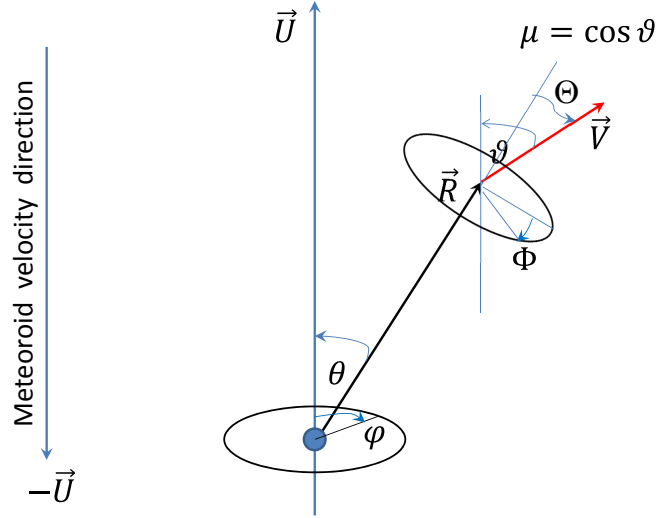


**Figure 1.** Nomenclature of spatial coordinates and velocity variables. The spatial variables  $R = |\vec{R}|$ ,  $\theta$ ,  $\varphi$  denote the radius and two angles of the spherical coordinate system with the origin at the meteoroid center and the major axis anti-parallel to the meteoroid velocity (shown on the left). All other variables pertain to the particle velocity space:  $V = |\vec{V}|$  is the particle speed,  $\vartheta$  is the polar angle of  $\vec{V}$  with respect to the local axis parallel to  $\vec{U}$ ,  $\Phi$  is the axial angle measured from the common  $\vec{U}$ - $\vec{R}$  plane;  $\Theta$  is the polar angle of  $\vec{V}$  with respect to the local radial distance  $\vec{R}$ .

The velocity distribution of secondary ions,  $f^{(2)}$ , is expressed as a function of three velocity variables that are invariants of the ion collisionless motion. These variables include the ion speed,  $V$ , the cosine of the angle between the ion velocity vector  $\vec{V}$  and  $\vec{U}$ ,  $\mu = \cos \vartheta$ , and a normalized angular momentum variable,  $R_0$ , which to the minimum distance between the ion trajectory and the meteoroid center,  $R_0 = R \sin \Theta$ , where  $\Theta$  is the polar angle of  $\vec{V}$  with respect to the local radius vector  $\vec{R}$ . The entire set of velocity-space variables also includes a discrete variable  $\sigma_R$  which takes two values,  $\pm 1$ , depend-

ing on the sign of the particle radial velocity,

$$V_R = \frac{dR}{dt} \equiv V \cos \Theta = \sigma_R \sqrt{1 - \frac{R_0^2}{R^2}} V. \quad (1)$$

The value of  $\sigma_R = +1$  corresponds to the outgoing particles,  $V_R > 0$ , while  $\sigma_R = -1$  corresponds to the incoming particles,  $V_R < 0$ . At any location, the entire distribution function is given by a sum of the two corresponding functions,

$$f^{(2)}(V, \mu, R_0; R, \theta) = \sum_{\sigma_R = \pm 1} f_{\sigma_R}^{(2)}(V, \mu, R_0; R, \theta). \quad (2)$$

The functions  $f_{\sigma_R}^{(2)}$  are non-zero provided  $\mu = \cos \vartheta > 0$ ; otherwise  $f_{\sigma_R}^{(2)} = 0$ ,

$$\begin{aligned} f_{\sigma_R}^{(2)}(V, R, \theta) \Big|_{\mu > 0} &= L_{\sigma_R} \delta \left( V - \frac{2m_\beta \mu U}{m + m_\beta} \right), \\ L_{\sigma_R} &= \frac{G_{\text{ion}}(U, 1 - 2\mu^2) n_0 n_A}{\sqrt{3} \mu U^2} \left( 1 + \frac{m}{m_\beta} \right)^3 I(R, R_0), \\ f_{\sigma_R}^{(2)}(V, R, \theta) \Big|_{\mu < 0} &= 0. \end{aligned} \quad (3)$$

The quantities  $n_0$  and  $n_A$  are the densities of the ablated particles at the meteoroid surface and of the atmospheric particles at a given altitude, respectively. The quantity  $G_{\text{ion}}(U, 1 - 2\mu^2)$  originates from the differential cross-section of ionizing collisions,  $G_{\text{ion}}$ , expressed as a function of the relative speed between the two colliding particles,  $u = |\vec{u}|$ , and the cosine of the scattering angle,  $\Theta_{\text{sc}}$ . In this paper, we simplify our treatment by assuming  $G_{\text{ion}}$  to be a function of only  $u \approx U$ . The corresponding angular dependence in the relevant energy range is generally unknown, but the assumption of isotropic  $G_{\text{ion}}(U)$  is reasonable.

The condition  $\mu > 0$  is fulfilled if either

$$\sigma_R = \text{sgn}(\cos \theta) \quad \text{and} \quad 0 < R_0 < R_c(\theta, \Phi) \quad (4a)$$

or

$$\sigma_R = -\text{sgn}(\cos \theta) \quad \text{and} \quad R_c(\theta, \Phi) < R_0 < R, \quad (4b)$$

where  $\text{sgn}(x)$  means the sign of  $x$  and

$$R_c(\theta, \Phi) = \frac{R |\cos \theta|}{\sqrt{1 - \sin^2 \theta \sin^2 \Phi}}. \quad (5)$$

Here  $\Phi$  is the axial angle of the particle velocity  $\vec{V}$  around the direction of the local radius-vector  $\vec{R}$  (see Figure 1) and we set the origin  $\Phi = 0$  where  $\vec{V}$  lies in the common  $\vec{R}$ - $\vec{U}$  plane.

In this paper, we consider the meteor plasma located not too close to the meteoroid,  $R \gg r_M$ . The corresponding multiplier  $I(R, R_0)$  in equation (3) has the following piecewise definition:

$$I(R, R_0) = \begin{cases} J_R^\infty & \text{for } \sigma_R = -1, \\ J_{R_0}^\infty + J_{R_0}^R = 2J_{R_0}^\infty - J_R^\infty & \text{for } \sigma_R = +1, \end{cases} \quad (6)$$

where, under constraints of  $R, R_0 > 3r_M$ , the well-convergent integral  $J_a^b$ , taken as a function of its integration limits,  $b > a \geq R_0$ , is given by

$$J_a^b \approx r_M^2 \int_a^b \left[ 1 + \left( \frac{R'}{\lambda_T^{(1)}} \right)^{2/3} \right] \exp \left[ -\frac{3}{2} \left( \frac{R'}{\lambda_T^{(1)}} \right)^{2/3} \right] \frac{dR'}{R' \sqrt{(R')^2 - R_0^2}}. \quad (7)$$

Here  $\lambda_T^{(1)}$  is the mean free path of the primary (ablated) particles,

$$\lambda_T^{(1)} = \frac{V_T}{\nu_T^{(1)}}, \quad V_T = \left( \frac{T_M}{m_M} \right)^{1/2}, \quad \nu_T^{(1)} \approx 2\pi n_A U \int_{-1}^1 G^{(1)}(U, \Lambda) d\Lambda, \quad (8)$$

where  $T_M$  and  $m_M$  are the temperature and mass of the primary meteor particles. The quantity  $G^{(1)}(U, \Lambda)$  includes all collisions that result in scattering of the primary neutral particles. The expression for  $G^{(1)}$ , as that for  $G_{\text{ion}}$ , takes into account that  $V_T \ll U$ , so that the collision frequency  $\nu_T^{(1)}$  depends only on the meteoroid speed,  $U$ , and hence is the same for all particles. This reduces  $\lambda_T^{(1)}$  to a constant value which becomes the characteristic length-scale of the near-meteoroid plasma.

The general integral  $J_a^b$  cannot be calculated exactly, but the particular integral  $J_{R_0}^\infty$  has an almost perfect analytic approximation,

$$J_{R_0}^\infty \approx \frac{\pi r_M^2}{2R_0} \sqrt{1 + \frac{2}{\pi} \left( \frac{R_0}{\lambda_T^{(1)}} \right)^{2/3}} \exp \left[ -\frac{3}{2} \left( \frac{R_0}{\lambda_T^{(1)}} \right)^{2/3} \right], \quad (9)$$

accurate within 1% for all  $R_0$ . As we demonstrate below, depending on the specific calculation, it may become beneficial to use either the exact original integral expression for  $J_a^b$  given by equation (7) or (only for  $J_{R_0}^\infty$ ) its approximation given by equation (9).

For local calculations of the ion density it is more convenient to pass from the invariant velocity variables  $V, R_0, \mu$  to local variables  $V, R_0, \Phi$ , where  $\Theta$  and  $\Phi$  are the polar and axial angles of the ion velocity about the direction of the local radius-vector  $\vec{R}$ , as depicted by Figure 1.

### 3 Plasma density calculations

Radar head echo is determined by the spatial distribution of the electron density around the meteoroid. The near-meteoroid plasma is quasi-neutral, so that the electron density almost equals that of ions,  $n_e \approx n_i = n$ . We calculate the spatial distribution of the ion density based on the distribution function explained in section 2.

The ion density can be easily calculated in the far region of  $R \gg \lambda_T^{(1)}$ . Albeit less simple, but  $n^{(2)}(R, \theta)$  can also be explicitly calculated in the opposite limit of  $R \ll \lambda_T^{(1)}$ . In the entire space of arbitrary  $R$ , we were unable to find a unified purely algebraic expression for  $n^{(2)}(R, \theta)$ . However, we have reduced the general 3D velocity-space integral to a much simpler expression for  $n^{(2)}$  in terms of normalized variables and parameters, as explained below. This universal expression involves only treatable analytical functions and two 1D integral functions suitable for simple numerical integration and tabulation. The resultant universal expression for  $n^{(2)}$  makes the future analysis and computer modeling of the radar signal much easier.

#### 3.1 Preliminary remarks

At a given location determined by  $R$  and  $\theta$ , the ion density is given by  $n^{(2)} = \sum_{\sigma_R = \pm 1} \int f_{\sigma_R}^{(2)} V^2 dV d\Omega$ , where  $d\Omega = d(\cos \Theta) d\Phi$  denotes the elementary volume of the local solid angle. Choosing instead of  $\Theta$  the new variable  $R_0 = R \sin \Theta$ , we obtain

$$n^{(2)} = \frac{1}{R} \sum_{\sigma_R = \pm 1} \int_0^R \frac{R_0 dR_0}{\sqrt{R^2 - R_0^2}} \int_0^{2\pi} d\Phi \int_0^\infty f_{\sigma_R}^{(2)} V^2 dV. \quad (10)$$

First, we integrate over  $V$  to eliminate the  $\delta$ -function in equation (3),

$$\int_0^\infty f_{\sigma_R}^{(2)} V^2 dV = \frac{4\mu G_{\text{ion}} n_0 n_A}{\sqrt{3}} \left( 1 + \frac{m}{m_\beta} \right) I(R, R_0). \quad (11)$$

As a result of this simple integration, the previously singular factor  $\mu$  in the expression for  $L_{\sigma_R}$  has moved from its denominator to the numerator, reducing dramatically the relative contribution of the ‘small-angle’ ( $\Theta_{\text{sc}} = 1 - 2\mu^2 \approx 1$ ,  $\mu \ll 1$ ) ionization where some assumptions of our general theory are invalid [Dimant and Oppenheim, 2016]. Since we assumed above isotropic  $G_{\text{ion}} = G_{\text{ion}}(U)$ , the only  $\Phi$ -dependent quantity in the right-hand side (RHS) of equation (11) is  $\mu$  in the numerator. This variable is expressed in terms of  $R_0$  and  $\Phi$  as

$$\mu = \sigma_R \sqrt{1 - \frac{R_0^2}{R^2}} \cos \theta + \frac{R_0 \sin \theta}{R} \cos \Phi. \quad (12)$$

The function  $I(R, R_0)$ , along with the corresponding integral expressions for  $J_a^b$ , are described by equations (6) to (9).

### 3.2 Long-distance asymptotics, $R \gg \lambda_T^{(1)}$ , behind the meteoroid

We start by calculating the ion density at the simplest limit of long radial distances,  $R \gg \lambda_T^{(1)}$ , behind the meteoroid. Ignoring exponentially small densities (as explained below), we will consider only the space behind the meteoroid,  $\cos \theta > 0$ . Outgoing particles within the dominant beam-like (along  $\vec{R}$ ) velocity distribution make the major contribution to  $n^{(2)}$ . In equations (10) and (11), setting  $R_0 \ll R$ ,  $\vartheta \approx \theta$ ,  $\mu \approx \cos \theta$ , while neglecting the exponentially small quantity  $J_{R_0}^\infty$  in equation (6), we obtain  $I(R, R_0) \approx 2J_{R_0}^\infty$ . This allows us to easily integrate the RHS of equation (10) over  $\Phi$ . In the exact integral expression given by (7), the primary contribution to  $J_{R_0}^\infty$  arises from components of  $f_+^{(2)}$  near the meteoroid,  $R' \lesssim \lambda_T^{(1)} \ll R$ . This allows us to extend the upper integration limit to infinity. This yields

$$\begin{aligned} n^{(2)} \Big|_{R \gg \lambda_T^{(1)}} &\approx \frac{16\pi r_M^2 G_{\text{ion}} n_0 n_A \cos \theta}{R^2 \sqrt{3}} \left(1 + \frac{m}{m_\beta}\right) \\ &\times \int_0^\infty R_0 dR_0 \int_{R_0}^\infty \left[1 + \left(\frac{R'}{\lambda_T^{(1)}}\right)^{2/3}\right] \exp\left[-\frac{3}{2} \left(\frac{R'}{\lambda_T^{(1)}}\right)^{2/3}\right] \frac{dR'}{R' \sqrt{(R')^2 - R_0^2}}. \end{aligned} \quad (13)$$

Changing here the order of integration with the corresponding adjustment of the integration limits,  $\int_0^\infty dR_0 \int_{R_0}^\infty (\dots) dR' = \int_0^\infty dR' \int_0^{R'} (\dots) dR_0$ , and using the simple identities

$$\begin{aligned} \int_0^{R'} \frac{R_0 dR_0}{\sqrt{(R')^2 - R_0^2}} &= R', \\ \int_0^\infty \left[1 + \left(\frac{R'}{\lambda_T^{(1)}}\right)^{2/3}\right] \exp\left[-\frac{3}{2} \left(\frac{R'}{\lambda_T^{(1)}}\right)^{2/3}\right] dR' &= \sqrt{\frac{2\pi}{3}} \lambda_T^{(1)}, \end{aligned}$$

we obtain for  $\cos \theta > 0$ :

$$n^{(2)} \Big|_{R \gg \lambda_T^{(1)}} \approx \frac{k r_M^2 \lambda_T^{(1)} G_{\text{ion}} n_0 n_A}{R^2} \left(1 + \frac{m}{m_\beta}\right) \cos \theta, \quad (14)$$

where  $k = 16\sqrt{2} \pi^{3/2}/3$ . Equation (14) shows that at  $R \gg \lambda_T^{(1)}$  the density of the major ion population fall off as  $(\cos \theta)/R^2$ .

If, however, instead of using the exact integral expression for  $J_{R_0}^\infty$  given by equation (7), we employed its approximation given by equation (9) then, applying the identity

$$\int_0^\infty \sqrt{\left(1 + \frac{4x}{3\pi}\right)} x \exp(-x) dx = \frac{\sqrt{3\pi}}{4} \exp\left(\frac{3\pi}{8}\right) K_1\left(\frac{3\pi}{8}\right), \quad (15)$$

deduced from [Gradshteyn and Ryzhik, 1994, equation 3.372], with the modified Bessel function of the second kind  $K_\nu(x)$ , we would obtain equation (14) with  $k$  replaced by a formally different coefficient,  $k_1 = (2^{\frac{3}{2}}\pi^{\frac{5}{2}}/\sqrt{3}) \exp(3\pi/8) K_1(3\pi/8)$ . However, the numerical values of  $k \approx 42$  and  $k_1 \approx 41.74$  are so close to each other that can be considered as essentially the same. This confirms that the approximate expression  $J_{R_0}^\infty$  given by equation (9) is reasonably accurate and can be successfully used in other occasions, as done below.

### 3.3 General distances

For all but largest meteors the radar head echo is formed within moderate radial distances of  $R \sim \lambda_T^{(1)}$ , the most difficult domain to treat analytically. Below, we reduce the general expression for  $n^{(2)}$  to a simpler form, more suitable for a further analytic or numerical treatment, and then obtain the explicit spatial distribution of  $n^{(2)}$  for  $R \ll \lambda_T^{(1)}$ , the limit opposite to that considered in section 3.2. After that, we will discuss the general case, using numerical integrations.

#### 3.3.1 Reduction of the general ion density

Under assumption of the isotropic differential cross-section,  $G_{\text{ion}}(U)$ , equation (11) involves  $\mu$  only as a linear multiplier. For the further analysis, equation (10) with the integration over  $\Phi$  is no longer convenient. More advantageous is integrating over  $\mu$ , where  $\mu$  is given by equation (12). Introducing a dimensionless variable

$$\xi_0 = \frac{R_0}{R} = \sin \Theta \leq 1 \quad (16)$$

and changing variables  $R_0, \Phi$  to  $\xi_0, \mu$ , we arrive at

$$n^{(2)} = 2 \times \frac{4n_0n_A}{\sqrt{3}} \left(1 + \frac{m}{m_\beta}\right) G_{\text{ion}}M \quad (17a)$$

$$M \equiv \sum_{\sigma_R=\pm 1} \int_0^1 \frac{I(R, \xi_0 R) \xi_0 d\xi_0}{\sqrt{1-\xi_0^2}} I_\mu(\xi_0), \quad (17b)$$

$$I_\mu(\xi_0) = \int \frac{H(\mu) \mu d\mu}{\sqrt{\xi_0^2 \sin^2 \theta - (\mu - \sigma_R \sqrt{1-\xi_0^2} \cos \theta)^2}}, \quad (17c)$$

where the function  $I(R, R_0)$  is given by equation (6) and  $H(x)$  is the Heaviside step-function ( $H(x) = 1$  for  $x \geq 0$  and  $H(x) = 0$  for  $x < 0$ ). The latter takes into account the fact that the distribution function of secondary particles is non-zero only for positive  $\mu$ , as discussed in Paper 1. The integration in  $I_\mu(\xi_0)$  is performed over the entire  $\mu$ -range where the expression under the square root is non-negative. The factor ‘2’ in front of the RHS of equation (17a) takes into account the fact that each value of  $\mu$  corresponds to two symmetric values of  $\Phi$  with the same  $\cos \Phi$  but opposite  $\sin \Phi$ . Introducing

$$\mu_1 = \sigma_R \sqrt{1-\xi_0^2} \cos \theta - \xi_0 \sin \theta, \quad \mu_2 = \sigma_R \sqrt{1-\xi_0^2} \cos \theta + \xi_0 \sin \theta, \quad (18)$$

and eliminating the step-function, we can rewrite  $I_\mu(\xi_0)$  in equation (17c) as

$$I_\mu(\xi_0) = \int_{\max(\mu_1, 0)}^{\max(\mu_2, 0)} \frac{\mu d\mu}{\sqrt{(\mu_2 - \mu)(\mu - \mu_1)}}, \quad (19)$$

where the integration limits take into account that in general case  $\mu_{1,2}$  can be negative. For all signs of  $\cos \theta$ , the relations between  $\mu_{1,2}$  and 0 are listed in this table:

		$\xi_0 <  \cos \theta $		$\xi_0 >  \cos \theta $		
$\sigma_R \cos \theta < 0$		$\mu_1 < \mu_2 < 0$		$\mu_1 < 0 < \mu_2$		.
$\sigma_R \cos \theta > 0$		$\mu_2 > \mu_1 > 0$		$\mu_1 < 0 < \mu_2$		

All this yields for  $I_\mu$ , defined by equation (17c), a piece-wise expression:

$$I_\mu(\xi_0) = \begin{cases} \int_{\mu_1}^{\mu_2} \frac{\mu d\mu}{\sqrt{(\mu_2-\mu)(\mu-\mu_1)}} & \text{if } \xi_0 < |\cos \theta| \text{ and } \sigma_R \cos \theta > 0, \\ \int_0^{\mu_2} \frac{\mu d\mu}{\sqrt{(\mu_2-\mu)(\mu-\mu_1)}} & \text{if } \xi_0 > |\cos \theta| \text{ for all } \sigma_R \cos \theta, \\ 0 & \text{if } \xi_0 < |\cos \theta| \text{ and } \sigma_R \cos \theta < 0. \end{cases} \quad (21)$$

Using the definitions given by equation (18), we obtain:

$$\int_{\mu_1}^{\mu_2} \frac{\mu d\mu}{\sqrt{(\mu_2-\mu)(\mu-\mu_1)}} = \pi \sigma_R \sqrt{1 - \xi_0^2} \cos \theta, \quad (22)$$

and (for  $\xi_0 > |\cos \theta|$ ):

$$\begin{aligned} & \int_0^{\mu_2} \frac{\mu d\mu}{\sqrt{(\mu_2-\mu)(\mu-\mu_1)}} \\ &= \sigma_R \left( \frac{\pi}{2} + \arcsin \frac{\sigma_R \sqrt{1 - \xi_0^2} \cos \theta}{\xi_0 \sin \theta} \right) \sqrt{1 - \xi_0^2} \cos \theta + \sqrt{\xi_0^2 - \cos^2 \theta}. \end{aligned} \quad (23)$$

Recalling equation (6), for the quantity  $M$ , defined by equation (17b), we obtain

$$\begin{aligned} M &= \int_0^1 \frac{(2J_{R_0}^\infty - J_R^\infty)_{\sigma_{R>0}} \xi_0 d\xi_0}{\sqrt{1 - \xi_0^2}} \int_{\max(\mu_1, 0)}^{\max(\mu_2, 0)} \frac{\mu d\mu}{\sqrt{(\mu_2 - \mu)(\mu - \mu_1)}_{\sigma_{R=+1}}} \\ &+ \int_0^1 \frac{(J_R^\infty)_{\sigma_{R<0}} \xi_0 d\xi_0}{\sqrt{1 - \xi_0^2}} \int_{\max(\mu_1, 0)}^{\max(\mu_2, 0)} \frac{\mu d\mu}{\sqrt{(\mu_2 - \mu)(\mu - \mu_1)}_{\sigma_{R=-1}}} \end{aligned} \quad (24)$$

Regrouping the terms, and using equations (21)–(23), for all  $\theta$  we obtain

$$\begin{aligned} M &= \pi |\cos \theta| \int_0^{|\cos \theta|} J_{R_0}^\infty \xi_0 d\xi_0 + (\pi \cos \theta) \int_0^1 J_{R_0}^R \xi_0 d\xi_0 \\ &+ 2 \int_{|\cos \theta|}^1 J_{R_0}^\infty \xi_0 \sqrt{\frac{\xi_0^2 - \cos^2 \theta}{1 - \xi_0^2}} d\xi_0 \\ &+ 2 |\cos \theta| \int_{|\cos \theta|}^1 J_{R_0}^\infty \xi_0 \arcsin \frac{\sqrt{1 - \xi_0^2} |\cos \theta|}{\xi_0 \sin \theta} d\xi_0, \end{aligned} \quad (25)$$

where  $J_{R_0}^R = J_{R_0}^\infty - J_R^\infty$ . All terms in the RHS of equation (25) are symmetric with respect to the sign of  $(\cos \theta)$ , except the second term which is antisymmetric. This term is responsible for the entire asymmetry between the locations in front of the meteoroid ( $\cos \theta < 0$ ) and behind it ( $\cos \theta > 0$ ).

To simplify further, we introduce other variables and parameters,

$$\eta = \frac{R'}{R}, \quad \beta = \left( \frac{R}{\lambda_T^{(1)}} \right)^{\frac{2}{3}}, \quad q = \frac{r_M^2}{R}, \quad (26)$$

where  $R'$  is the integration variable in  $J_a^b$ , defined by equation (7). With use of these dimensionless quantities, equation (7) yields

$$J_{R_0}^\infty = q \int_{\xi_0}^\infty \left( 1 + \beta \eta^{\frac{2}{3}} \right) \exp \left( - \frac{3\beta \eta^{\frac{2}{3}}}{2} \right) \frac{d\eta}{\eta \sqrt{\eta^2 - \xi_0^2}}, \quad (27a)$$

$$J_{R_0}^R = q \int_{\xi_0}^1 \left( 1 + \beta \eta^{\frac{2}{3}} \right) \exp \left( - \frac{3\beta \eta^{\frac{2}{3}}}{2} \right) \frac{d\eta}{\eta \sqrt{\eta^2 - \xi_0^2}}. \quad (27b)$$



For some calculations, we will also need approximate equation (9) for  $J_{R_0}^\infty$ ,

$$J_{R_0}^\infty \approx \frac{\pi q}{2\xi_0} \sqrt{1 + \frac{2}{\pi} \beta \xi_0^{\frac{2}{3}} \exp\left(-\frac{3}{2} \beta \xi_0^{\frac{2}{3}}\right)}. \quad (28)$$

For  $J_{R_0}^R$  we need no approximations, as will become clear soon.

Before proceeding, we check that the long-distance limit of  $R \gg \lambda_T^{(1)}$  (i.e.,  $\beta \gg 1$ ) for the above equations provides a smooth transition to the range of long distances considered in section 3.2. Beyond a narrow vicinity around  $\theta = \pi/2$ , given by  $|\cos \theta| \lesssim \beta^{-3/2}$ , we can easily see that in the RHS of equation (25) the third and fourth terms are exponentially small. Neglecting them and extending the same accuracy to the upper integration limit in the first and second terms,  $J_{R_0}^R \approx J_{R_0}^\infty$ , we obtain

$$M|_{\beta \gg 1} \approx \begin{cases} 2\pi (\cos \theta) \int_0^\infty J_{R_0}^\infty \xi_0 d\xi_0 & \text{if } \cos \theta > 0, \\ 0 & \text{if } \cos \theta < 0. \end{cases} \quad (29)$$

Using for  $J_{R_0}^\infty$  the exact equation (27a) and applying for the double integration the same approach as in section 3.2, we obtain

$$M|_{\beta \gg 1} \approx \frac{2\pi q \cos \theta}{\beta^{\frac{3}{2}}} \sqrt{\frac{2\pi}{3}}.$$

Returning from the temporary dimensionless parameters  $\beta, q$  to the original coordinate  $R$  and inserting the corresponding  $M$  to equation (17a), for  $\cos \theta > 0$  we recreate equation (14).

### 3.3.2 Short distances, $R \ll \lambda_T^{(1)}$

Now we consider the short-distance limit of  $R \ll \lambda_T^{(1)}$  ( $\beta \ll 1$ ) which is opposite to that discussed in section 3.2. For not too large integration variables  $R', \eta = R'/R \ll \beta^{-3/2}$ , all factors with  $\beta \eta^{\frac{2}{3}}$  in equation (27) can be neglected. Since this range of  $R'$  makes the dominant contribution to all integrals, we extend this approximation to the entire range of  $\eta$ , so that

$$J_{R_0}^\infty \approx q \int_{\xi_0}^\infty \frac{d\eta}{\eta \sqrt{\eta^2 - \xi_0^2}} = \frac{\pi q}{2\xi_0}, \quad (30a)$$

$$J_{R_0}^R \approx q \int_{\xi_0}^1 \frac{d\eta}{\eta \sqrt{\eta^2 - \xi_0^2}} = \frac{q}{\xi_0} \arccos \xi_0. \quad (30b)$$

In this limit, the first two terms in the RHS of equation (25) can be easily integrated, yielding  $\pi q [\pi(\cos^2 \theta)/2 + \cos \theta]$ . The two remaining terms can be expressed in terms of the complete elliptic integrals of the 1st and 2nd kind,

$$K(k) = \int_0^1 \frac{dt}{\sqrt{(1-t^2)(1-k^2 t^2)}}, \quad E(k) = \int_0^1 \sqrt{\frac{1-k^2 t^2}{1-t^2}} dt, \quad (31)$$

respectively, where  $0 \leq k < 1$ . Indeed, for constant  $\xi_0 J_{R_0}^\infty$ , as in equation (30a), the third term in equation (25) becomes proportional to

$$I_1 = \int_{|\cos \theta|}^1 \sqrt{\frac{\xi_0^2 - \cos^2 \theta}{1 - \xi_0^2}} d\xi_0.$$

This integral already resembles an elliptic integral, but reducing  $I_1$  to those with the real arguments requires additional efforts. Substituting  $\xi_0 = \sqrt{1 - z^2 \sin^2 \theta}$ , we reduce  $I_1$

to  $E(\sin \theta) - (\cos^2 \theta) K(\sin \theta)$ . In a similar way, we can also calculate the fourth term in equation (25). With constant  $J_{R_0}^\infty \xi_0$ , this term becomes proportional to

$$I_2 = \int_{|\cos \theta|}^1 \arcsin \frac{\sqrt{1 - \xi_0^2} |\cos \theta|}{\xi_0 \sin \theta} d\xi_0.$$

Integration of the corresponding indefinite integral by parts gives

$$\begin{aligned} & \int \arcsin \frac{\sqrt{1 - \xi_0^2} |\cos \theta|}{\xi_0 \sin \theta} d\xi_0 \\ &= \xi_0 \arcsin \frac{\sqrt{1 - \xi_0^2} |\cos \theta|}{\xi_0 \sin \theta} + |\cos \theta| \int \frac{d\xi_0}{\sqrt{(1 - \xi_0^2)(\xi_0^2 - \cos^2 \theta)}}. \end{aligned}$$

Making the same substitution for the remaining integral in the RHS as done for  $I_1$  and evaluating everything over the proper integration limits, we obtain  $I_2 = (K(\sin \theta) - \pi/2)|\cos \theta|$ . When adding all terms in the RHS of equation (25), the  $K(\sin \theta)$ -terms in  $I_{1,2}$  cancel and equation (17b) reduces to a simple expression:  $M \approx \pi q[\cos \theta + E(\sin \theta)]$ . As a result, the ion density in the short-distance limit reduces to

$$n^{(2)} \Big|_{R \ll \lambda_T^{(1)}} \approx \frac{8\pi r_M^2 G_{\text{ion}} n_0 n_A}{\sqrt{3} R} \left( 1 + \frac{m}{m_\beta} \right) [\cos \theta + E(\sin \theta)]. \quad (32)$$

Comparing equation (32) with the opposite limit given by equation (14) shows that the  $1/R^2$ -dependency of  $n^{(2)} \Big|_{R \gg \lambda_T^{(1)}}$  transforms to the  $1/R$ -dependency for  $n^{(2)} \Big|_{R \ll \lambda_T^{(1)}}$ . The angular  $\theta$ -dependency also changes significantly. While in the long-distance limit of  $R \gg \lambda_T^{(1)}$  ions occupy almost entirely the half-space behind the meteoroid ( $0 \leq \theta < \pi/2$ ), in the short-distance limit of  $R \ll \lambda_T^{(1)}$  ions show a noticeable presence in front of the meteoroid ( $\pi/2 \leq \theta \leq \pi$ ) as well. Red dashed curves in Figure 2 show the corresponding angular dependencies normalized to their maximum values at  $\theta = 0$ .

### 3.3.3 Arbitrary distances

The case of moderate distances  $R \sim \lambda_T^{(1)}$  is covered by general equations (17) and (25) with  $J_{R_0}^\infty$  and  $J_{R_0}^R$  expressed in the original integral form by equation (27), or in an approximate, but explicit, form for  $J_{R_0}^\infty$  by equation (28). Unlike  $J_{R_0}^\infty$ , the integral  $J_{R_0}^R$  is involved only in the second term in the RHS of equation (25). As we show below, this term can be calculated exactly by using the integral form of equation (27b). Below we obtain the explicit analytic expressions for the first and second terms in the RHS of equation (25). Being unable to obtain a general analytic approximation for the two last integral terms, we will integrate them numerically.

*3.3.3.1 First term in equation (25).* Using equation (27a), for the integral in the first term of the expression for  $M$  in (25), we have

$$\begin{aligned} Q_1 &\equiv \frac{1}{q} \int_0^{|\cos \theta|} J_{R_0}^\infty \xi_0 d\xi_0 \\ &= \int_0^{|\cos \theta|} \left[ \int_{\xi_0}^\infty \left( 1 + \beta \eta^{\frac{2}{3}} \right) \exp \left( -\frac{3\beta \eta^{\frac{2}{3}}}{2} \right) \frac{d\eta}{\eta} \right] \frac{\xi_0 d\xi_0}{\sqrt{\eta^2 - \xi_0^2}}, \end{aligned} \quad (33)$$

where the dimensionless variables  $\eta$ ,  $\beta$ , and  $q$  are defined by equation (26). Changing the order of integration, we obtain

$$\begin{aligned} Q_1 &= \int_0^{|\cos \theta|} \left( 1 + \beta \eta^{\frac{2}{3}} \right) \exp \left( -\frac{3\beta \eta^{\frac{2}{3}}}{2} \right) \frac{d\eta}{\eta} \int_0^\eta \frac{\xi_0 d\xi_0}{\sqrt{\eta^2 - \xi_0^2}} \\ &+ \int_{|\cos \theta|}^\infty \left( 1 + \beta \eta^{\frac{2}{3}} \right) \exp \left( -\frac{3\beta \eta^{\frac{2}{3}}}{2} \right) \frac{d\eta}{\eta} \int_0^{|\cos \theta|} \frac{\xi_0 d\xi_0}{\sqrt{\eta^2 - \xi_0^2}}. \end{aligned}$$

These integrations yield

$$Q_1 = \sqrt{\frac{2\pi}{3\beta^3}} \operatorname{erf}\left(\sqrt{\frac{3\beta}{2}} |\cos\theta|^{\frac{1}{3}}\right) + J_1 - \left(|\cos\theta|^{\frac{2}{3}} + \frac{2}{\beta}\right) |\cos\theta|^{\frac{1}{3}} \exp\left(-\frac{3\beta |\cos\theta|^{\frac{2}{3}}}{2}\right), \quad (34)$$

where  $\operatorname{erf}(x) = (2/\sqrt{\pi}) \int_0^x e^{-x^2} dx$  is the standard error-function and

$$J_1 = \int_{|\cos\theta|}^{\infty} \left(1 + \beta\eta^{\frac{2}{3}}\right) \exp\left(-\frac{3\beta\eta^{\frac{2}{3}}}{2}\right) \left(1 - \sqrt{1 - \frac{|\cos\theta|^2}{\eta^2}}\right) d\eta. \quad (35)$$

The integral  $J_1$  cannot be taken exactly, but directly below we obtain its approximate value. However, even without doing this, one can easily verify that equations (34) and (35) provide both the correct limit of short distances,  $\lim_{\beta \rightarrow 0} Q_1 = \pi |\cos\theta|/2$ , and the large-distance asymptotics of  $\beta \gg 1$ ,  $Q_1 \approx (2\pi/3)^{1/2} \beta^{-3/2}$ .

Now we find an approximate expression for  $J_1$  by constructing a proper analytic interpolation between two limiting cases. For small  $\beta$ , we have

$$J_1|_{\beta \rightarrow 0} = \left(\frac{\pi}{2} - 1\right) |\cos\theta|. \quad (36)$$

In the opposite limit of large  $\beta$ , the major contribution to the integral  $J_1$  is made in the small vicinity of the lower integration limit. This yields the following asymptotics,

$$J_1 \approx \left(1 - \sqrt{\frac{\pi}{2\beta |\cos\theta|^{\frac{2}{3}}}}\right) \exp\left(-\frac{3\beta |\cos\theta|^{\frac{2}{3}}}{2}\right) |\cos\theta|. \quad (37)$$

Interpolating between equations (36) and (37) as

$$J_1 \approx \left(1 - \frac{(4 - \pi) \sqrt{2\pi}}{2\sqrt{2\pi + (4 - \pi)^2 \beta |\cos\theta|^{\frac{2}{3}}}}\right) \exp\left(-\frac{3\beta |\cos\theta|^{\frac{2}{3}}}{2}\right) |\cos\theta|, \quad (38)$$

we obtain a reasonably good approximation for  $J_1$ , valid in the entire range of  $\beta$ . Even in the worst case of  $\beta |\cos\theta|^{\frac{2}{3}} \sim 6$ , the mismatch between the actual integral value and this approximation is only  $\simeq 6\%$ .

Combining equations (34) with (38), for the double integral  $Q_1$  defined by equation (33), to a good accuracy we obtain

$$Q_1 \approx \sqrt{\frac{2\pi}{3\beta^3}} \operatorname{erf}\left(\sqrt{\frac{3\beta}{2}} |\cos\theta|^{\frac{1}{3}}\right) - \left[\frac{(4 - \pi) \sqrt{2\pi} |\cos\theta|}{2\sqrt{2\pi + \beta (4 - \pi)^2 |\cos\theta|^{\frac{2}{3}}}} + \frac{2 |\cos\theta|^{\frac{1}{3}}}{\beta}\right] \exp\left(-\frac{3\beta |\cos\theta|^{\frac{2}{3}}}{2}\right). \quad (39)$$

*3.3.3.2 Second term in equation (25).* Now we calculate the integral

$$Q_2 \equiv \frac{1}{q} \int_0^1 J_{R_0}^R \xi_0 d\xi_0 = \int_0^{|\cos\theta|} \left[ \int_{\xi_0}^1 \left(1 + \beta\eta^{\frac{2}{3}}\right) \exp\left(-\frac{3\beta\eta^{\frac{2}{3}}}{2}\right) \frac{d\eta}{\eta} \right] \frac{\xi_0 d\xi_0}{\sqrt{\eta^2 - \xi_0^2}}. \quad (40)$$

Unlike  $Q_1$ , this integral can be calculated exactly. Indeed, changing the order of integration, we obtain

$$\begin{aligned}
 Q_2 &= \int_0^1 \left(1 + \beta\eta^{\frac{2}{3}}\right) \exp\left(-\frac{3\beta\eta^{\frac{2}{3}}}{2}\right) \frac{d\eta}{\eta} \int_0^\eta \frac{\xi_0 d\xi_0}{\sqrt{\eta^2 - \xi_0^2}} \\
 &= \int_0^1 \left(1 + \beta\eta^{\frac{2}{3}}\right) \exp\left(-\frac{3\beta\eta^{\frac{2}{3}}}{2}\right) d\eta \\
 &= \sqrt{\frac{2\pi}{3\beta^3}} \operatorname{erf}\left(\sqrt{\frac{3\beta}{2}}\right) - \left(1 + \frac{2}{\beta}\right) \exp\left(-\frac{3\beta}{2}\right). \tag{41}
 \end{aligned}$$

*3.3.3.3 Density along the major axis.* Now we consider two particular positions along the major axis: strictly behind the meteoroid ( $\theta = 0$ ) and strictly in front of it ( $\theta = \pi$ ). In both these positions, we have  $|\cos\theta| = 1$ , so that the third and fourth terms in the RHS of equation (25) become zero. The combination of the two first terms there is given by

$$\pi |\cos\theta| \int_0^{|\cos\theta|} J_{R_0}^\infty \xi_0 d\xi_0 + \pi (\cos\theta) \int_0^1 J_{R_0}^R \xi_0 d\xi_0 = \pi q (|\cos\theta| Q_1 + (\cos\theta) Q_2) \tag{42}$$

As a result, at the major axis behind the meteoroid we obtain

$$\begin{aligned}
 n^{(2)}\Big|_{\theta=0} &= \frac{8\pi r_M^2 n_0 n_A}{R\sqrt{3}} \left(1 + \frac{m}{m_\beta}\right) G_{\text{ion}} \left\{ 2\sqrt{\frac{2\pi}{3}} \frac{\lambda_T^{(1)}}{R} \operatorname{erf}\left[\sqrt{\frac{3}{2}} \left(\frac{R}{\lambda_T^{(1)}}\right)^{\frac{2}{3}}\right] \right. \\
 &\quad \left. - \left[ \frac{(4-\pi)\sqrt{2\pi}}{2\sqrt{2\pi + (4-\pi)^2 (R/\lambda_T^{(1)})^{\frac{2}{3}}}} + 1 + 4 \left(\frac{\lambda_T^{(1)}}{R}\right)^{\frac{2}{3}} \right] \exp\left[-\frac{3}{2} \left(\frac{R}{\lambda_T^{(1)}}\right)^{\frac{2}{3}}\right] \right\}. \tag{43}
 \end{aligned}$$

Similarly, at the major axis in front of the meteoroid we obtain

$$\begin{aligned}
 n^{(2)}\Big|_{\theta=\pi} &= \frac{8\pi r_M^2 n_0 n_A}{R\sqrt{3}} \left(1 + \frac{m}{m_\beta}\right) G_{\text{ion}} \\
 &\quad \times \left[ 1 - \frac{(4-\pi)\sqrt{2\pi}}{2\sqrt{2\pi + (4-\pi)^2 (R/\lambda_T^{(1)})^{\frac{2}{3}}}} \right] \exp\left[-\frac{3}{2} \left(\frac{R}{\lambda_T^{(1)}}\right)^{\frac{2}{3}}\right]. \tag{44}
 \end{aligned}$$

Figure 3 shows these two radial dependencies with  $\cos\theta = 1$  ( $\theta = 0$ ) and  $\cos\theta = -1$  ( $\theta = \pi$ ) are actually representative for slightly more general  $\cos\theta$ . The radial-distance dependencies for positive and negative  $\cos\theta$  look qualitatively different, as we discuss below.

Behind the meteoroid,  $\cos\theta > 0$ , the radial dependence of the density gradually changes from  $n^{(2)} \propto 1/R$  for  $R \ll \lambda_T^{(1)}$ , as described by equation (32), to  $n^{(2)} \propto 1/R^2$  for  $R \gg \lambda_T^{(1)}$ , as described by equation (14). This change in the power-law radial dependence of  $n^{(2)}$  occurs for the following reason. The source for the secondary ions are the primary neutral particles, whose density falls off near the meteoroid roughly as  $1/R^2$ . At a given location  $R$ , the number of ions moving in a certain direction is determined by the total collisional ionization over the preceding segment of the straight-line trajectory aligned with that direction. For  $R \ll \lambda_T^{(1)}$ , the total integration over the entire ionization path acquires an additional factor  $\propto R$  which gradually transforms  $1/R^2$  to  $1/R$ . On the other hand, for  $R \gg \lambda_T^{(1)}$  only localized ionization within  $R' \lesssim \lambda_T^{(1)}$  plays a role, resulting in ‘saturation’ of the previous additional factor  $R$  at a constant value  $\sim \lambda_T^{(1)}$ . This leaves the  $\propto 1/R^2$  dependence of  $n^{(2)}$  essentially untouched. This transition works only for locations behind the meteoroid,  $\cos\theta > 0$ , because almost all freshly born

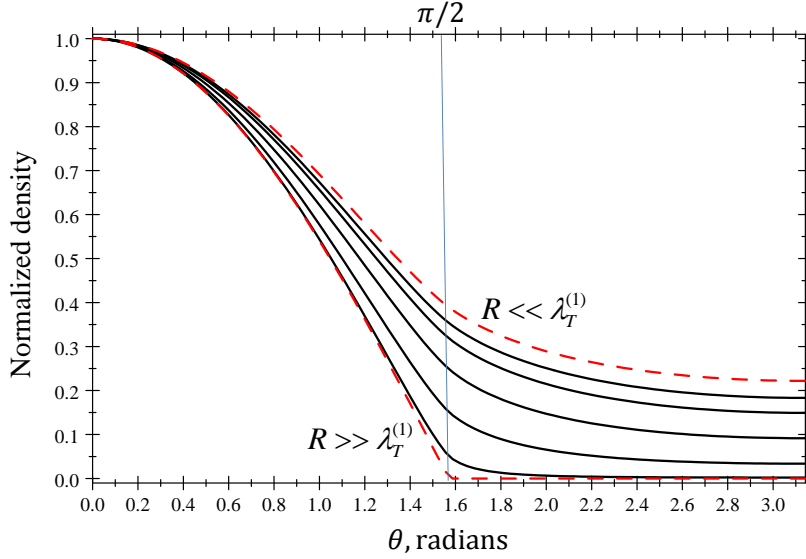


**Figure 2.** Density versus the polar angle  $\theta$  for different distances (black solid curves from the top to the bottom:  $R/\lambda_T^{(1)} = 0.1; 0.3; 1; 3; 10$ ). Red dashed curves show asymptotic solutions given by equation (29) (the top curve) and by equation (32). All density distributions are normalized to the maximum values strictly behind the meteoroid,  $\theta = 0$  (see Fig. 3).

ions have velocities  $\vec{V}$  with positive  $\mu = \cos \vartheta$ , where  $\vartheta$  is the angle between  $\vec{V}$  and  $-\vec{U}$ , as shown in Figure 1. Regardless of how far away from the meteoroid this  $R, \theta$ -point is located, all preceding straight-line trajectory segments with  $\mu > 0$  always cross the near-meteoroid volume  $R' \lesssim \lambda_T^{(1)}$ ,

A significantly different situation takes place in front of the meteoroid,  $\cos \theta < 0$ . At  $R \ll \lambda_T^{(1)}$ , straight-line trajectory segments with  $\mu > 0$  also cross a part of the near-meteoroid volume  $R' \lesssim \lambda_T^{(1)}$ . That is why here  $n^{(2)}|_{\theta=\pi}$  is quite noticeable, although a few times smaller than  $n^{(2)}|_{\theta=0}$ . On the other hand, at larger distances,  $R \gtrsim \lambda_T^{(1)}$ , there are almost no preceding trajectory segments with positive  $\mu$  that would cross the near region of  $R' \lesssim \lambda_T^{(1)}$ . These trajectories cross the regions where the number of the primary particles is itself exponentially small, so that  $n^{(2)}|_{\theta=\pi} \propto \exp[-(3/2)(R/\lambda_T^{(1)})^{2/3}]$ . This exponentially decreasing density remains much less than that behind the meteoroid where  $n^{(2)}$  decreases largely by a power law.

*3.3.3.4 General case.* For the general case of  $R \sim \lambda_T^{(1)}$  with  $\cos \theta \neq \pm 1$ , we were unable to find acceptable analytic approximations for the two last (integral) terms in the RHS of equation (25). Therefore, we will integrate those 1D integrals numerically.

Now we summarize the entire expression for  $n^{(2)}$  by combining equation (17a) with (25), where in the first two terms the integrals  $\int_0^{|\cos \theta|} J_{R_0}^\infty \xi_0 d\xi_0 = qQ_1$  and  $\int_0^1 J_{R_0}^R \xi_0 d\xi_0 = qQ_2$  were calculated with  $Q_{1,2}$  explicitly given by equations (39) and (41) (as it was done above when calculating the ion density at the major axis). For the two remaining integral terms in equation (25) we use the approximation for  $J_{R_0}^\infty$  given by equation (28). This

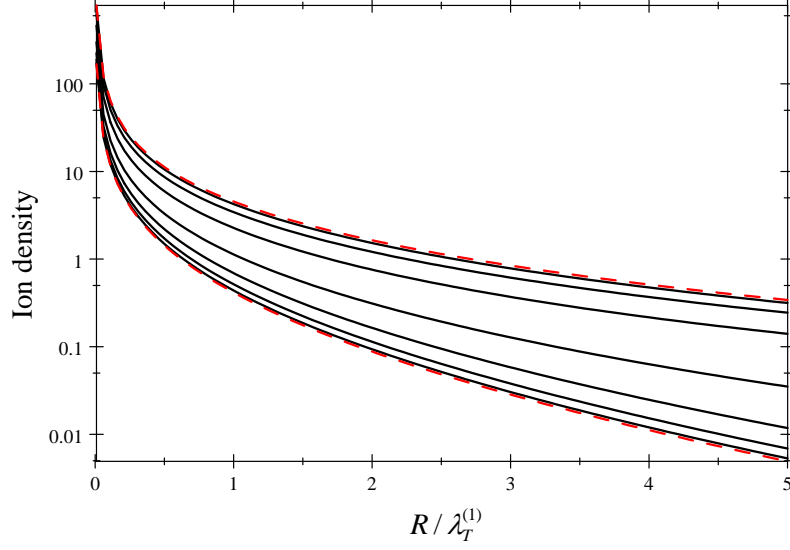


**Figure 3.** Normalized density versus the relative radial distance,  $R/\lambda_T^{(1)}$ , for several equally separated angles  $\theta$ . The normalization corresponds to the factor  $M$  with  $q \rightarrow \lambda_T^{(1)}/R$ . Red dashed curves for  $\theta = 0$  (the top curve) and for  $\theta = \pi$  (the bottom curve) are described analytically by equations (43) and (44), respectively. Black solid curves show  $M(R, \theta)$  obtained by combining analytic equations (33) and (40) for the two first terms of equation (25) with numerically calculated two remaining integral terms. The black solid curves, from the top to the bottom, correspond to  $\theta = \pi/8; \pi/4; 3\pi/8; \pi/2; 5\pi/8; 3\pi/4$ ; and  $7\pi/8$ , respectively. The black solid curves with  $\theta = \pi/8$  and  $\theta = 7\pi/8$  are almost indistinguishable from the top and bottom red dashed curves,  $\theta = 0, \pi$ .

gives

$$n^{(2)} = \frac{8\pi r_M^2 n_0 n_A}{\sqrt{3}R} \left(1 + \frac{m}{m_\beta}\right) G_{\text{ion}}(U) \times [f_1(R, \cos \theta) |\cos \theta| + f_2(R) \cos \theta + f_3(R, \cos \theta)], \quad (45)$$

where

$$f_1(R, \cos \theta) = \frac{\lambda_T^{(1)}}{R} \sqrt{\frac{2\pi}{3}} \operatorname{erf} \left[ \sqrt{\frac{3}{2}} \left( \frac{R}{\lambda_T^{(1)}} \right)^{\frac{1}{3}} |\cos \theta|^{\frac{1}{3}} \right] - \left[ \frac{(4 - \pi) |\cos \theta|}{2\sqrt{1 + (4 - \pi)^2 (R/\lambda_T^{(1)})^{\frac{2}{3}} |\cos \theta|^{\frac{2}{3}}}} / (2\pi) + 2 \left( \frac{\lambda_T^{(1)}}{R} \right)^{\frac{2}{3}} |\cos \theta|^{\frac{1}{3}} \right] \times \exp \left[ -\frac{3 |\cos \theta|^{\frac{2}{3}}}{2} \left( \frac{R}{\lambda_T^{(1)}} \right)^{\frac{2}{3}} \right], \quad (46)$$

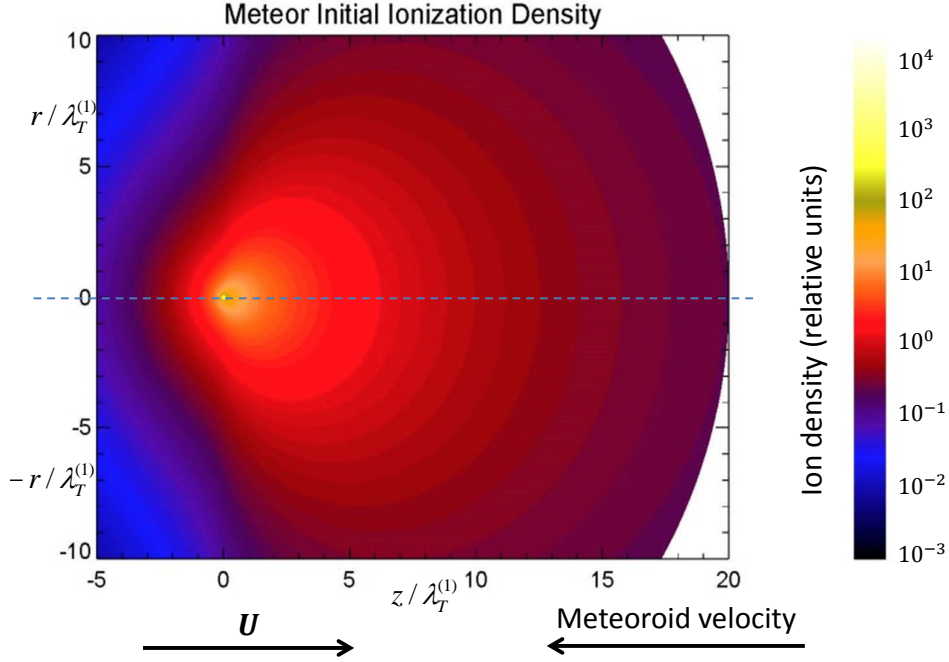


**Figure 4.** Spatial distribution of plasma density around a small meteoroid. The figure shows a cross-section of an axially symmetric distribution by a plane that includes the symmetry axis (blue dashed line). The meteoroid is shown by a small white circle at the symmetry axis. The color coding signifies the plasma density in relative units;  $r$  is the distance to the symmetry axis.

$$f_2(R) = \frac{\lambda_T^{(1)}}{R} \sqrt{\frac{2\pi}{3}} \operatorname{erf} \left[ \sqrt{\frac{3}{2}} \left( \frac{R}{\lambda_T^{(1)}} \right)^{\frac{1}{3}} \right] - \left[ 1 + 2 \left( \frac{\lambda_T^{(1)}}{R} \right)^{\frac{2}{3}} \right] \exp \left[ -\frac{3}{2} \left( \frac{R}{\lambda_T^{(1)}} \right)^{\frac{2}{3}} \right], \quad (47)$$

$$f_3(R, \cos \theta) = \int_{|\cos \theta|}^1 \sqrt{1 + \frac{2\xi_0^{\frac{2}{3}}}{\pi} \left( \frac{R}{\lambda_T^{(1)}} \right)^{\frac{2}{3}} \exp \left[ -\frac{3\xi_0^{\frac{2}{3}}}{2} \left( \frac{R}{\lambda_T^{(1)}} \right)^{\frac{2}{3}} \right]} \times \sqrt{\frac{\xi_0^2 - \cos^2 \theta}{1 - \xi_0^2}} d\xi_0 + |\cos \theta| \int_{|\cos \theta|}^1 \sqrt{1 + \frac{2\xi_0^{\frac{2}{3}}}{\pi} \left( \frac{R}{\lambda_T^{(1)}} \right)^{\frac{2}{3}} \exp \left[ -\frac{3\xi_0^{\frac{2}{3}}}{2} \left( \frac{R}{\lambda_T^{(1)}} \right)^{\frac{2}{3}} \right]} \times \arcsin \frac{\sqrt{1 - \xi_0^2} |\cos \theta|}{\xi_0 \sqrt{1 - \cos^2 \theta}} d\xi_0. \quad (48)$$

For the isotropic differential cross-section the mean free path defined equation by equation (8) reduces to

$$\lambda_T^{(1)} = \frac{1}{4\pi U n_A G(U)} \left( \frac{T_M}{m_M} \right)^{1/2}. \quad (49)$$

Figures 2, 3, and 4 illustrate the general  $\theta, R$ -dependences of  $n^{(2)}$ .

As might be expected, in Figure 2 the normalized curves with intermediate values of  $R/\lambda_T^{(1)}$  smoothly and uniformly fill the gap between the two asymptotic solutions corresponding to the long,  $R \gg \lambda_T^{(1)}$ , and short,  $R \ll \lambda_T^{(1)}$ , distances, as described by equations (14) and (32). Similarly, in Figure 3 the curves with intermediate values of  $\cos \theta$  fill the gap between the solutions strictly in front of the meteoroid ( $\cos \theta = -1$ ) and behind it ( $\cos \theta = 1$ ), as described by equations (44) and (43).

Figure 4 shows the entire 3D structure of the ion density in color coding. Since the spatial distribution of the plasma density is axially symmetric, this figure shows a meridional cross-section that includes the major axis. Behind the meteoroid, at  $z \equiv R \cos \theta \gg \lambda_T^{(1)}$  the presented distribution may be inaccurate because it does not properly describe the extended trail formed lagging behind multiply scattered ions. However, around the meteoroid this distribution should be reasonably accurate. Figure 4 shows a significant span in the density values (seven orders of magnitude). Notice visible bulges in constant density contours in front of the meteoroid. This feature has not been predicted in previous PIC simulations [Dyrud *et al.*, 2008a,b].

## 4 Discussion

The spatial structure of the near-meteoroid plasma shown in Figure 4 scales with the collisional mean free path of the primary (ablated) particles,  $\lambda_T^{(1)}$ . The latter, in turn, scales with the altitude( $h$ )-dependent atmospheric density as  $\lambda_T^{(1)} \propto 1/n_A(h)$ . The frontal edge of the meteoroid plasma has a bulge located around the major axis at the distance  $\sim \lambda_T^{(1)}$  from the meteoroid.

The most striking feature of the meteor-plasma spatial structure is not the angular dependence of  $n^{(2)}$  but rather the fact that near the meteoroid,  $R \lesssim \lambda_T^{(1)}$ , the plasma density behaves as  $n^{(2)} \simeq F(\theta)/R$ . The singular  $1/R$  dependence holds almost to the meteoroid surface,  $R \sim r_M$ . This fact has serious implications for head-echo observations and for the corresponding modeling of the radar wave propagation.

To analyze radio wave propagation through the dense meteoroid plasma with  $n_e \approx n_i \approx n^{(2)} \gg n_A$ , we apply the simplest criterion of geometrical optics applicable (the WKB approximation):

$$\frac{\lambda_0}{2\pi} \frac{|\nabla \tilde{n}|}{|\tilde{n}|^2} \ll 1 \quad (50)$$

[Ginzburg, 1971]. Here  $\lambda_0 = c/f$  is the vacuum wavelength with the frequency  $f$ , and index of refraction (neglecting the geomagnetic field) given by  $\tilde{n} = (1 - n_e/n_{\text{cr}})^{1/2}$ , where

$$n_{\text{cr}} = \frac{4\pi^2 \epsilon_0 m_e f^2}{e^2} \approx 1.24 \times 10^4 \text{ cm}^{-3} \left( \frac{f}{1 \text{ MHz}} \right)^2 \quad (51)$$

is the critical plasma density corresponding to  $\tilde{n} = 0$ .

Most of small meteoroids have a radius within the hundreds-of-microns range, i.e., many orders of magnitude less than the mean free path,  $\lambda_T^{(1)}$ . This means that the radar beam with the wave frequency in the tens-of-MHz range (e.g., Jicamarca with  $f = 50$  MHz) will almost certainly cross the boundary  $R = R_{\text{cr}}(\theta)$  where  $n_{\text{cr}} = n_e \approx n^{(2)}(R_{\text{cr}}, \theta)$ . Under the geometric-optics approximation, the boundary  $R \approx R_{\text{cr}}(\theta)$  represents the wave reflection level.

According to equation (50), geometric optics applies beyond the wave reflection level of  $\tilde{n} = 0$  and, for  $n_e \propto 1/R$ , where

$$R \gg \sqrt{\frac{\lambda_0 R_{\text{cr}}}{4\pi |\tilde{n}|^3}}. \quad (52)$$



For small radii,  $R \ll R_{\text{cr}}$ , for which  $|\tilde{n}| \approx (R_{\text{cr}}/R)^{1/2} \gg 1$ , this requires  $R \gg \lambda_0^2/(16\pi^2 R_{\text{cr}})$ , meaning that geometric optics applicability will necessarily fail in the close proximity to the meteoroid.

If  $R_{\text{cr}} \gg \lambda_0/(4\pi)$  then the radio wave propagating from larger to smaller  $R$  will reach the reflection level of the plasma density,  $R = R_{\text{cr}}$ , well before reaching the volume where the WKB becomes invalid. This corresponds to normal overdense reflection of the radar wave, so that the  $1/R$  dependence of  $n^{(2)}$  will not prevent using the regular geometric-optics technique. If, however,  $R_{\text{cr}} \lesssim \lambda_0$  then the applicability of the geometric-optics propagation breaks down before the radio wave reaches its reflection level. This requires modeling the radar wave propagation using full Maxwell's equations [Marshall and Close, 2015]. The characteristics of the radar signal obtained in this way may differ from those obtained in the framework of the regular ray tracing.

To conclude this discussion, we note that in the underlying kinetic theory we have neglected the effect of fields on the ion collisionless motion. Directly near the meteoroid, where the calculated density sharply increases with decreasing  $R$  this assumption may become invalid. This is especially true within the Debye length from the meteoroid surface, where one may expect a significant net positive charge formed by slow ions after fast electrons moved away from that region. This charge separation can create a significant potential barrier for electrons that, at the same time, will accelerate ions away from the meteoroid. This may modify the  $1/R$  rate near the meteoroid surface. However, the relevant distances are typically much smaller than the radar wavelength, so that this localized modification should not affect the overall radio wave propagation and formation of the radar head echo.

## 5 Conclusions

Based on the kinetic theory developed in the companion paper [Dimant and Oppenheim, 2016], we have calculated the spatial distribution of the meteor plasma responsible for the radar head echo.

The underlying theory assumes that (1) plasma electrons obey the Boltzmann distribution; (2) most plasma ions originate from the ablated meteoroid material after exactly one ionizing collision, while further collisions can be neglected; (3) the ion motion between collisions is largely unaffected by fields. In order to make plasma density calculations easier, in this paper we have additionally assumed the isotropic differential cross-section of the meteor-particle ionization.

Equations (45) to (48) describe the entire spatial distribution of the near-meteoroid plasma density. Figures 2, 3, and 4 illustrate the solution. The major feature of the near-meteoroid plasma density spatial distribution is its dominant  $1/R$  dependence in most of the plasma. This quasi-singular behavior makes the radar penetrated near-meteoroid plasma to be overdense at locations sufficiently close to the meteoroid. This and other features are important for modeling the radar head echo. In near future, we are planning to employ the obtained plasma density distribution for such modeling.

## Acknowledgments

This work was supported by NSF Grant AGS-1244842.

## References

Bronshthen, V. A. (1983), *Physics of Meteoric Phenomena*, Reidel Publishing Company, Dordrecht-Boston-Lancaster.

- Campbell-Brown, M. D., and S. Close (2007), Meteoroid structure from radar head echoes, *Mon. Not. R. Astron. Soc.*, *382*, 1309–1316, doi:10.1111/j.1365-2966.2007.12471.x.
- Ceplecha, Z., J. Borovička, W. G. Elford, D. O. Revelle, R. L. Hawkes, V. Porubčan, and M. Šimek (1998), Meteor Phenomena and Bodies, *Space Sci. Rev.*, *84*, 327–471, doi:10.1023/A:1005069928850.
- Close, S., M. Oppenheim, D. Durand, and L. Dyrud (2005), A new method for determining meteoroid mass from head echo data, *J. Geophys. Res.*, *110*, A09,308, doi:10.1029/2004JA010950.
- Dimant, Y. S., and M. M. Oppenheim (2016), Formation of dense plasma around a small meteoroid: 1. Kinetic theory, *ArXiv: 1608.08524*.
- Dyrud, L., D. Wilson, S. Boerve, J. Trulsen, H. Pecseli, S. Close, C. Chen, and Y. Lee (2008a), Plasma and Electromagnetic Simulations of Meteor Head Echo Radar Reflections, *Earth Moon and Planets*, *102*, 383–394, doi: 10.1007/s11038-007-9189-8.
- Dyrud, L., D. Wilson, S. Boerve, J. Trulsen, H. Pecseli, S. Close, C. Chen, and Y. Lee (2008b), Plasma and electromagnetic wave simulations of meteors, *Advances in Space Research*, *42*, 136–142, doi:10.1016/j.asr.2007.03.048.
- Ginzburg, V. L. (1971), *The propagation of electromagnetic waves in plasmas*, Pergamon Press, Oxford.
- Gradshteyn, I. S., and I. M. Ryzhik (1994), *Table of Integrals, Series, and Products*, Academic Press, San Diego.
- Marshall, R. A., and S. Close (2015), An FDTD model of scattering from meteor head plasma, *J. Geophys. Res.*, *120*, 5931–5942, doi:10.1002/2015JA021238.